First Observation of Mercury Species on an Important Water Vapor Channel in the Southeast Tibetan Plateau

Huiming Lin[1], Yindong Tong[2*], Chenghao Yu[1], Long Chen[3], Xiufeng Yin[4], Qianggong Zhang[5,6], Shichang Kang[4,6], Lun Luo[7], James Schauer[8,9], Benjamin de Foy[10], Xuejun Wang[1**]

Affiliations

1. MOE Laboratory of Earth Surface Processes, College of Urban and Environmental Sciences, Peking University, Beijing 100871, China;

2. School of Environmental Science and Engineering, Tianjin University, Tianjin, 300072, China;

3. School of Geographic Sciences, East China Normal University, Shanghai 200241, China;

4. State Key Laboratory of Cryospheric Science, Northwest Institute of Eco-Environment and Resources, Chinese Academy of Sciences, Lanzhou 730000, China

5. Key Laboratory of Tibetan Environment Changes and Land Surface Processes, Institute of Tibetan Plateau Research, Chinese Academy of Sciences, Beijing, 100101, China;

6. CAS Center for Excellence in Tibetan Plateau Earth Sciences, Beijing, 100085, China;

7. South-East Tibetan plateau Station for integrated observation and research of alpine environment,CAS

8. Department of Civil and Environmental Engineering, University of Wisconsin-Madison, Madison, WI, USA;

9. Wisconsin State Laboratory of Hygiene, University of Wisconsin-Madison, WI, USA;

10. Department of Earth and Atmospheric Sciences, Saint Louis University, St. Louis, MO, 63108, USA

Correspondence:

*Yindong Tong, Tianjin University, Tianjin, China, Email at: yindongtong@tju.edu.cn;

**Xuejun Wang, Peking University, Beijing, China, Email at: wangxuejun@pku.edu.cn

Abstract

The Tibetan Plateau is generally considered to be a significantly clean area owing to its high altitude; however, the transport of atmospheric pollutants from the Indian subcontinent to the Tibetan Plateau has infected the Tibetan environments. Nyingchi is located at the end of an important water vapor channel. In this study, continuous monitoring of gaseous elemental mercury (GEM), gaseous oxidized mercury (GOM), and particle-bound mercury (PBM) was conducted in Nyingchi from March 30 to September 3, 2019, to study the influence of the Indian summer monsoon (ISM) on the origin, transport and behavior of mercury. The atmospheric Hg concentrations during the preceding Indian summer monsoon (PISM) period (1.20 ± 0.35 ng m^{-3}, 13.5 ± 7.3 pg m^{-3}, and 11.4 ± 4.8 pg m^{-3} for GEM, GOM, and PBM, respectively) were relatively higher than those during the ISM period (0.95 ± 0.21 ng m^{-3}, 12.7 ± 14.3 pg m^{-3} and 8.8 ± 6.0 pg m^{-3}). The average annual total gaseous mercury concentration in the Nyingchi region was obtained using a passive sampler as 1.12 ± 0.28 ng m^{-3}. The GEM concentration showed that the sampling area was very clean. The GEM has several patterns of daily variation during different periods. Stable high GEM

39 concentrations occur at night during PISM, which may be related to the nocturnal boundary layer. High

40 values occurring in the late afternoon during the ISM may be related to long-range transport. The results

41 of the trajectory model demonstrate that the sources of pollutants at Nyingchi are different under the

42 control of different airflow fields. During westerly circulation, pollutants mainly originate from northeast

43 India or Nepal. During the ISM period, the pollutants mainly originate from northeast India, or the Bay

44 of Bengal, and the Indian Ocean. The strong precipitation and vegetation effects on Hg during the ISM

45 resulted in low Hg concentrations transmitted to Nyingchi during this period. Further, principal

46 component analysis showed that long-distance transport, local emissions, meteorological factors, and

47 snowmelt factors are the main factors affecting the local Hg concentration in Nyingchi.

48

49 **1. Introduction**

50   Mercury (Hg) is classified as a hazardous pollutant because it is bio-accumulative and toxic.

51 Generally, atmospheric Hg can be categorized into three major types: gaseous elemental mercury (GEM),

52 gaseous oxidized mercury (GOM), and particle-bound mercury (PBM) (Selin, 2009). The stable chemical

53 properties of GEM coupled with its long atmospheric lifetime (approximately 0.3 to 1 year) makes GEM

54 an important global pollutant (Selin, 2009;Travnikov et al., 2017). In contrast, GOM and PBM are easily

55 removed from the atmosphere through wet and dry deposition because of their chemical activity, and

56 have significant impacts on the local environment (Lindberg and Stratton, 1998;Seigneur et al., 2006).

57 Both GOM and PBM have complex fundamental physiochemical properties and may have complicated

58 relationships with other regional pollutants (Gustin et al., 2015). Understanding, identifying, and

59 characterizing Hg sources and their global and regional transport mechanisms is crucial for global

60 atmospheric Hg control and health effect research (UNEP, 2018). Since 2013, the Minamata Convention

61 was established to control the global mercury pollution (UNEP, 2013a). Monitoring atmospheric Hg is

62 an important prerequisite for implementing the convention. Currently, several Hg monitoring networks

63 and studies have been established to better understand atmospheric Hg cycling. The Atmospheric

64 Mercury Network (AMNet; Gay et al., 2013), Global Mercury Observation System (GMOS), and the

65 Canadian Atmospheric Mercury Network (CAMNet) are the main monitoring networks operating in

66 North America and Europe; majority of them only monitor GEM concentrations (Gay et al.,

67 2013;Sprovieri et al., 2013;Sprovieri et al., 2016;Kellerhals et al., 2003). Researchers worldwide have

68 also contributed to monitoring the data from different regions (Gustin et al., 2015;Jiang and Wang,

69 2019;Stylo et al., 2016). However, there exists some gaps in understanding the sources and transport of

70 atmospheric Hg in some remote areas, especially in harsh environmental areas where performing

71 monitoring is difficult.

72   Considering that GEM can be transported globally over long distances and that the transport

73 distances of GOM and PBM vary greatly in different environments, atmospheric Hg concentration

74 monitoring may not directly reflect the intensity of regional atmospheric Hg emissions. Our previous

75 study of the Qomolangma National Nature Preserve (QNNP) (Lin et al., 2019) demonstrated that the Hg

76 emitted from India can cross the Himalayas to reach the Tibetan Plateau. Further research on the

77 transboundary transport of Hg should be conducted to better understand the transport mechanisms. This

78 is particularly true in Asia, where the environmental pollution is generally severe. China and India are

79   reported to be the world's largest consumers of coal (BP Statistical Review of World Energy, 2018).
80   Considering that coal is the largest source of Hg in the atmosphere (approximately 86% of Hg comes
81   from fuel combustion (Chen et al., 2016)), both China and India have great Hg emission potential. Further
82   research on pollutant transport in Asia should be conducted to support policy development and
83   responsibility allocation.

84   The Tibetan Plateau, with an average elevation of more than 4,000 m above sea level, is a natural
85   barrier between inland China and the Indian subcontinent (Qiu, 2008;Lin et al., 2019). In the southern
86   part of the Tibetan Plateau, the Himalayas, with an average altitude of 6,000 m, can serve as a solid
87   barrier to pollutant transport. However, this barrier cannot completely block the transboundary
88   transportation of pollutants according to previous studies. The transboundary and long-distance transport
89   of pollutants across the Himalayas has attracted considerable attention (Wang et al., 2018;Zhang et al.,
90   2015a;Yang et al., 2018;Li et al., 2016;Feng et al., 2019;Zhu et al., 2019). Several studies have shown
91   that the transboundary intrusion of atmospheric pollutants through the Himalayas on the Tibetan Plateau
92   is crucial for many pollutants (Yang et al., 2018;Li et al., 2016;Zhang et al., 2015b;Pokhrel et al.,
93   2016;Lin et al., 2019). Zhang et al. (2017) studied short-lived reactive aromatic hydrocarbons and
94   indicated that the cut-off low system that have lower altitude in the Himalayas is a major pathway for
95   long-distance transport of aromatic hydrocarbons in the Tibetan Plateau. Persistent organic pollutants
96   have been reported to be transported to the interior of the Tibetan Plateau by traveling along valleys or
97   across ridges (Gong et al., 2019a). The transport of aerosols and organic pollutants along the most
98   important water vapor channel, the Yarlung Zangbu/Brahmaputra Grand Canyon (hereafter referred to as
99   the YZB Grand Canyon), has been observed (Wang et al., 2015;Sheng et al., 2013). Our previous study
100 in the QNNP, on the southern border of the Tibetan Plateau, proved that atmospheric Hg from the Indian
101 subcontinent can be transported across high-altitude mountains directly to the Tibetan Plateau under the
102 action of the Indian monsoon and local glacier winds (Lin et al., 2019). However, to the best of our
103 knowledge, the monitoring of the passage of atmospheric Hg in the water vapor channel—the YZB Grand
104 Canyon, into the Tibetan Plateau has not been conducted. Through the water vapor and airflow channel,
105 air masses carrying large amounts of water vapor as well as pollutants may enter Tibet, resulting in heavy
106 precipitation during the monsoon season. Huang et al. (2015) reported that the total Hg wet deposition
107 in Nyingchi, located in the YZB Grand Canyon, was lower than that in other Tibetan Plateau regions,
108 and the concentration was lower in the monsoon season than in the non-monsoon season. As an important
109 transport channel for summer monsoon moisture into China (Xu et al., 2020;Feng and Zhou, 2012;Yang
110 et al., 2013), the amount of water vapor transported into Tibet through this channel is considerable, and
111 the transport of pollutants needs further investigation.

112   In this study, we set up high-precision Hg species monitoring in Nyingchi, southeastern Tibetan
113 Plateau, covering both PISM and ISM periods. Hg passive sampling was also applied to cover the
114 monitoring of the entire year. To the best of our knowledge, this is the first monitoring study of
115 atmospheric Hg species in the most important water vapor channel of the Tibetan Plateau. To better
116 identify the sources of Hg pollution and potential pollution areas, we combined real-time Hg monitoring
117 data with backward trajectory analysis, cluster analysis, and potential source contribution function (PSCF)
118 analysis. We also collected other pollutant concentrations and rainfall data near the monitoring station

119   during the same period to better analyze the source and transport characteristics of Hg. By combining the

120   real-time monitoring data and model simulations, we attempted to better characterize the process of Hg

121   entering Tibet through the water vapor channel, which could allow researchers to further analyze the

122   transport of Hg from the Indian subcontinent into Tibet and provide scientific support for managerial

123   decision making.

2. Materials and methods

2.1 Atmospheric Hg monitoring site

126   Atmospheric Hg monitoring was performed at the South-East Tibetan Plateau Station for Integrated

127   Observation and Research of Alpine Environment (SET station, Figure 1) in Nyingchi, Tibet, China. The

128   SET station is located in the southeastern part of the Tibetan Plateau (29°45′59N, 94°44′16E, 3263 m

129   a.s.l.), in a water vapor transportation channel, from the Ganges River Plain to the Tibetan Plateau.

130   Nyingchi is mainly under the control of westerly winds (from September to April) and ISM (from May

131   to August), exhibiting sharp seasonal variations. The average annual air temperature is 5.6 °C. The

132   Tibetan Plateau is generally a moisture sink in summer (Feng and Zhou, 2012;Xu et al., 2020), with

133   climatological moisture originating from the Indian Ocean and the Bay of Bengal intruding into the center

134   of the Tibetan Plateau along the water vapor channels. The average annual precipitation is approximately

135   700-1000 mm at the SET station. During the westerly control period, the air masses are mainly from mid-

136   latitude inland areas with less water vapor, while during the ISM period, a large amount of water vapor

137   from the Indian Ocean enters Tibet. The precipitation begins at the foot of the YZB Grand Canyon and

138   is sustained along with the canyon into Tibet (Gong et al., 2019b), and the precipitation in the downstream

139   Motuo County is more than twice that of the Nyingchi area (Ping and Bo, 2018). The unique

140   geomorphological conditions and the effect of the strong monsoon have resulted in a unique high-altitude

141   distribution pattern of various biomes and vegetation in the area. The SET station is 75 km from Bayi

142   Town, where the capital of Nyingchi Prefecture is located, and 480 km from Lhasa, which is the capital

143   city of the Tibet Autonomous Region. Owing to the high altitude and harsh living environment, the

144   permanent population in Tibet is extremely small and only a few local pollutant emission sources have

145   been observed (UNEP, 2013b;UNEP, 2018).

2.2 GEM, GOM and PBM active monitoring

147   Real-time continuous measurements of GEM, GOM, and PBM concentrations were carried out

148   using Tekran Model 2537B, 1130, and 1135 instruments (Tekran Inc., Toronto, Canada) at the SET station

149   from April 1, 2019, to September 4, 2019, which could show the diurnal and daily changes in atmospheric

150   Hg concentration in detail. During the operation of the Tekran instruments, the sampling inlet was set at

151   ~1.5 m above the instrument platform (shown in Figure S1). Considering the high altitude at which the

152   instrument was installed, as well as to mitigate the impacts of low atmospheric pressures on the pump's

153   operation, a low air sampling rate of 7 L min^{-1} for the pump model and 0.75 L min^{-1} (at standard pressure

154   and temperature) for model 2537B were applied, based on the previous studies (Swartzendruber et al.,

155   2009;Zhang et al., 2015a;Zhang et al., 2016;Lin et al., 2019). Air was sucked from the atmosphere in the

156   Tekran instrument, and the Hg was divided into GOM, PBM, and GEM inside the instrument for analysis.

157   Every 60 min, GOM was enriched on a KCL-coated annular denuder, PBM was enriched on a quartz

158   fiber filter (QFF), and GEM was directly enriched on the gold tube of the Tekran 2537B. The collected

159   PBM and GOM were desorbed in succession to Hg(0) at temperatures of 800 °C and 500 °C in the

160   following hour, respectively. Hg(0) was then measured by cold vapor atomic fluorescence spectroscopy

161   (CVAFS) in the Tekran 2537B instrument. To ensure high data quality, the Tekran 2537B analyzer was

162   set to use the internal Hg source for automatic calibration every 23 h. The instrument was calibrated

163   using an external Hg source at the beginning and end of the monitoring period. The Tekran ambient Hg

164   analyzer has been described in detail in previous studies (Landis et al., 2002;Rutter et al., 2008;de Foy

165   et al., 2016;Lin et al., 2019). The monitoring data were also modified using the method from Slemr et al.

166   (2016) as previous studies suggested that there may be a low bias for low sampling loads (Slemr et al.,

167   2016;Ambrose, 2017).

2.3 Passive sampling of GEM concentration

169   Passive samplers were set up at the same station during and after the active monitoring period to

170   better reflect the long-term pattern of local GEM concentration changes from April 2019 to March 2020.

171   Sulfur-impregnated carbon (Calgon Carbon Corporation) was used as the sorbent for GEM (Guo et al.,

172   2014;Zhang et al., 2012;Tong et al., 2016;Lin et al., 2017). Passive samplers were deployed in triplicate

173   near the Tekran instrument at a height of ~2 m above the ground, and generally the passive samplers were

174   replaced three times per month. After sampling, all samplers were sealed in a three-layer zip-lock bag

175   and transported to the laboratory, where they were then measured with the DMA-80 (Milestone Inc.,

176   Itália). The passive sampling method has been successfully applied to the Tibetan Plateau (Guo et al.,

177   2014;Tong et al., 2016) and North China (Zhang et al., 2012) in past studies. The use and quality control

178   of the Hg passive sampler have been described in detail in our previous studies (Zhang et al., 2012;Guo

179   et al., 2014;Lin et al., 2017).

2.4 Meteorological data and other pollutants data

181   During the monitoring period, the local temperature (with a precision of 0.1 °C), relative humidity

182   (with a precision of 1%), wind speed (with a precision of 0.1 m s^{-1}), wind direction (with a precision of

183   1°), air pressure (with a precision of 0.1 hPa), solar radiation (with a precision of 1 W m^{-2}), and UV index

184   (with a precision of 0.1 MEDs) were recorded at a 5-minute resolution by the Vantage Pro2 weather

185   station (Davis Instruments, USA).

186   Hourly measurement data of $PM_{2.5}$, PM_{10}, SO_2, NO_2, O_3, and CO concentrations and AQI index

187   were obtained from a nearby monitoring station in Nyingchi, which was hosted by the China Ministry of

188   Ecology and Environment and published by the China National Environmental Monitoring Center. The

189   measurements were conducted following the technical regulations for the selection of ambient air quality

190   monitoring stations (National Environmental Protection Standards HJ 664-2013) (Yin et al., 2019).

2.5 Backward trajectory simulation

192   To better understand the source of atmospheric Hg, the Hybrid Single-Particle Lagrangian

193   Integrated Trajectory (HYSPLIT) model was applied to calculate the backward trajectory many

194   atmospheric particles (Stein et al., 2015;Chai et al., 2017;Chai et al., 2016;Hurst and Davis, 2017;Lin et

195   al., 2019). HYSPLIT was developed by the US National Oceanic and Atmospheric Administration

196   (NOAA) and is a known tool for explaining atmospherically transported, dispersed, and deposited of

197   particles. The HYSPLIT model (https://www.arl.noaa.gov/hysplit/hysplit/) is a hybrid method that

198   combines the Lagrangian and Euler approaches. The Lagrangian method calculates the movement of

199 matter under the action of advection and diffusion, and the Euler method uses a fixed three-dimensional
200 grid to calculate the pollutant concentration. The backward trajectory simulation used Global Data
201 Assimilation System (GDAS) data with 1°x1° latitude and longitude horizontal spatial resolution and 23
202 vertical levels at 6 h intervals. The trajectory arrival height was set to 1000 m a.g.l. Every backward
203 trajectory was stimulated for 72 h at 6 h intervals, which can cover China, Nepal, India, Pakistan, and
204 the majority of western Asia. Cluster analysis was performed after the trajectory calculation. Cluster
205 analysis can summarize the concentrations of GEM and the main trajectories from all trajectories.

206 The PSCF model was used to calculate the conditional probability by calculating the endpoints of
207 the trajectory segment ending in each cell, and the PSCF links the residence time in upwind areas with
208 measured high concentrations (Ashbaugh et al., 1985;Hopke and Association, 2016). The value of PSCF
209 represents the possibility that emissions from the source area will affect the air quality of the sampling
210 site. In this study, we used PSCF to identify the possible source region of atmospheric GEM in Nyingchi.
211 The PSCF values were also scaled by an arbitrary weighting function to reduce uncertainty owing to the
212 low PSCF value (Polissar et al., 1999).

213 **2.6 Principal components analyses**

214 Principal component analysis (PCA) is a data reduction method that can group some measured
215 variables into a few factors that can represent the behavior of the whole dataset (Jackson, 2005). PCA
216 has been employed in many previous Hg studies to analyze the relationships between Hg and multiple
217 pollutants and meteorological variables (Brooks et al., 2010;Cheng et al., 2012;Liu et al., 2007;Zhou et
218 al., 2019). All variables were normalized by standard deviation prior to running the PCA. To ensure that
219 PCA is a suitable method for the data set, the Kaiser-Meyer-Olkin measure of sampling adequacy (MSA >
220 0.5) and Bartlett's test of sphericity ($p < 0.05$) tests were performed during the data analysis process.
221 Total variance and scree plots after rotation were used in the PCA analysis to determine the factor
222 numbers. Components with variance ≥1.0 were retained. Variables with high factor loadings (generally >
223 0.5) were used to interpret the potential Hg source.

224 **3. Results and discussion**

225 **3.1 Species Hg concentrations in Nyingchi**

226 During the whole monitoring period, the GEM, GOM and PBM concentrations at SET station were
227 1.01 ± 0.27 ng m^{-3}, 12.8 ± 13.3 pg m^{-3}, and 9.3 ± 5.9 pg m^{-3}(mean±SD), respectively. Figure 2 shows the
228 GEM, GOM, and PBM concentrations and daily rainfall over the sampling period. Table S1 summarizes
229 the statistical metrics of species Hg, meteorological factors, and other pollutants. To further discuss the
230 patterns of Hg concentrations, the entire monitoring period was divided into the PISM period (before
231 May 1) and the ISM period. The ISM period was further subdivided into three periods (ISM1 – ISM3)
232 according to changes in precipitation. The atmospheric Hg concentrations during the PISM period
233 (1.20 ± 0.35 ng m^{-3}, 13.5 ± 7.3 pg m^{-3}, and 11.4 ± 4.8 pg m^{-3}, for GEM, GOM and PBM respectively) were
234 higher than those during the ISM period (0.95 ± 0.21 ng m^{-3}, 12.7 ± 14.3 pg m^{-3}, and 8.8 ± 6.0 pg m^{-3}, for
235 GEM, GOM and PBM respectively). During the PISM period, the locally monitored GEM concentrations
236 decreased continuously as the Indian monsoon developed and intensified (Figure 2), which may indicate
237 a change in the local Hg source as the decisive wind field changes from westerly to Indian monsoon.
238 GEM concentrations remained relatively stable during ISM1 and ISM2 (0.92 ± 0.23 to 0.92 ± 0.18 ng m^{-3}),

239 which may indicate that the source of GEM was relatively stable during this period. However, at the end

240 of the monsoon (ISM3), the GEM concentration started to increase gradually to 1.04±0.21 ng m^{-3}. There

241 was no significant correlation between GEM concentration and precipitation during the ISM period,

242 which may be due to the stable chemical properties of GEM because the air mass sources are relatively

243 stable during the ISM period (Horowitz et al., 2017), while GOM and PBM concentrations are strongly

244 influenced by precipitation (Figure 2). With the increase in rainfall from 113.75 mm during ISM1 period

245 to 373.28 mm during ISM2 period, the concentrations of GOM and PBM decreased sharply from

246 15.4±7.9 pg m^{-3} and 18.2±29.2 pg m^{-3} to 7.9±3.4 pg m^{-3} and 13.5±5.5 pg m^{-3}, respectively. The

247 considerable precipitation increase may be responsible for the rapidly reduced GOM and PBM

248 concentrations, as they are easily deposited in the atmosphere with precipitation (Lindberg and Stratton,

249 1998;Seigneur et al., 2006). In a previous study, Huang et al. (2015) found that even with heavy rain

250 during the monsoon period, the total Hg concentration in precipitation in the SET region was small but

251 still considerable, suggesting that there may be a stable source of Hg in the SET region during the ISM

252 period.

253   Figure 3 shows the results of the GEM concentrations obtained through passive samplers throughout

254 the year. The average GEM concentration is 1.12±0.28 ng m^{-3}, which is slightly higher than the average

255 GEM concentration during the Tekran monitoring period. The average GEM concentration is lower

256 (1.02±0.09 ng m^{-3}) during the ISM control period (from May to August) and higher during the westerly

257 circulation control period (1.16±0.32 ng m^{-3}); however, the GEM concentration during westerly

258 circulation control period has large fluctuations. Since there are almost no local industries and less human

259 activity in Nyingchi, this difference may indicate a higher input of pollutants introduced by westerly

260 circulation. For the variation throughout the year, the GEM concentration in May and June is the lowest

261 with an average concentration of only 0.97±0.18 ng m^{-3}, while November and December have the highest

262 GEM concentrations (1.24±0.37 ng m^{-3}).

263   Table 1 summarizes the GEM, GOM, and PBM concentrations from research papers of high-altitude

264 regions around the world. Compared to other high-altitude sites, the Hg concentrations in the SET region

265 were relatively low and did not reach the average Hg concentration level in the Northern Hemisphere (~

266 1.5-1.7 ng m^{-3}). Compared to previous studies of high elevation (> 2000 m a.s.l) regions, only Concordia

267 Station in Antarctica had lower GEM concentrations than those observed at the SET station. Ev-K2, Nam

268 Co, Qomolangma, and Shangri-La, the nearest monitoring stations to the SET station and at higher

269 altitudes, had higher GEM concentrations than those at the SET station. In particular, the GEM

270 concentration at Shangri-La was more than two-fold of that at the SET station. The differences in the

271 GEM concentrations among them may be mainly due to their different climatic conditions and different

272 monsoon control zones, which result in different pollutant source regions and air mass transport

273 trajectories. The Shangri-La station may be influenced by anthropogenic emissions within and outside

274 China, and therefore, has higher GEM concentrations. For Ev-K2 and Qomolangma stations, which are

275 under the influence of the ISM, they may be directly exposed to air masses with high concentrations of

276 pollutants transported from India and Nepal. Although there are violent deposition processes during the

277 climbing process to both Ev-K2 and Qomolangma stations, some Hg may survive reach the stations (Lin

278 et al., 2019). The GOM concentrations at the SET station were approximately at the average level among

279 the monitored sites. PBM concentrations were relatively low at the SET station, which may be due to the

280 high rainfall in the YZB Grand Canyon, easily washing away particulate Hg by rainwater.

281   The lower GEM concentrations during the ISM period may indicate that the pollutant sources of the

282 SET region changed with the weakening of the westerly circulation and the strengthening of the Indian

283 monsoon. In previous studies (Lin et al., 2019;Gong et al., 2019a;Wang et al., 2015), it is generally

284 believed that pollutants from the heavily polluted Indian subcontinent may be transported to the Tibetan

285 Plateau under the action of ISM, resulting in increased local pollutant concentrations on the plateau. This

286 was verified at the Qomolangma, Nam Co, and Mt. Ailao stations, where GEM concentrations were

287 higher during the ISM period than the PISM period (Lin et al., 2019;Yin et al., 2018;Zhang et al., 2016).

288 However, in our study, the SET station observed lower species Hg concentrations during the ISM than

289 the PISM period. For GEM, the decrease in concentration may be due to the absorption effect from the

290 dense vegetation during the monsoon period (Fu et al., 2016), while air masses from the Indian Ocean

291 bring large amounts of halogens, which may react with and deplete GEM. For GOM and PBM, increased

292 concentrations were observed during the ISM1 period, whereas their concentrations decreased sharply

293 during the ISM2 and ISM3 periods. The decreases in GOM and PBM concentrations may be mainly due

294 to the rapid increase in local precipitation during the Indian monsoon period, which starts after the

295 monsoon enters China from northwestern India. A large amount of water vapor from the Indian monsoon

296 climbs more than 3,000 m within ~100 km in the YZB Grand Canyon, producing considerable

297 precipitation. Therefore, GOM and PBM may settle during transportation and are unable to reach the

298 Nyingchi area.

299 **3.2 Diurnal Variation**

300   Figure 4 shows the diurnal variation of species Hg and the concentrations of other pollutants during

301 the entire monitoring period. In general, the species Hg concentrations varied significantly during the

302 PISM period, and the diurnal variation was relatively small after entering the ISM period. During the

303 PISM period, the GEM concentrations were relatively low during the daytime (average 1.07 ng m^{-3} from

304 11:00 to 18:00), gradually accumulated after sunset, and finally reached a relatively stable high value

305 (average 1.26 ng m^{-3}) at night. During the ISM period, the GEM concentration variation pattern was not

306 as pronounced as during the PISM period, with the lowest GEM concentration of the day usually

307 occurring around sunrise (0.83, 0.80, 0.88 ng m^{-3} for ISM1-3, respectively). During ISM1, the GEM

308 concentration reached a high value around 9:00 a.m., fluctuated less during the daytime, reached a

309 maximum value in the evening, and gradually dissipated in the early morning. During ISM2, the

310 maximum value was reached at approximately 16:00, was more stable in the evening, and gradually

311 dissipated in the early morning. During ISM3, the maximum value was reached at approximately 20:00

312 and dissipated in the early morning. The average of the daily maximum values were 1.04, 1.00, 1.16 ng

313 m^{-3} for ISM1-3 periods, respectively. After midnight, GEM concentrations gradually decreased. In

314 general, the daily variation of GEM in previous research were about 0.2-0.9 ng m^{-3} globally, and were

315 lower at the SET site (0.21, 0.20, 0.28 for ISM1-3 periods, respectively). For GOM and PBM, the diurnal

316 variations showed U-shaped variation patterns during the PISM period. During this period, the

317 concentrations of GOM and PBM reached low values between 10:00 and 14:00, then gradually

318 accumulated and peaked around midnight. After midnight, the concentration gradually decreased to its

319   lowest point. During the ISM1 period, GOM and PBM concentrations were higher in the afternoon and

320   evening, and showed a decreasing trend after midnight. During ISM2-3, GOM and PBM did not show

321   clear daily variation patterns. Except for the ISM2 period, there was little difference between GOM and

322   PBM concentrations during the other periods, which may be due to similar sources and behavioral

323   patterns in the environment. In contrast, during the ISM2 period, more precipitation (Figure 2) led to a

324   sharp decrease in PBM concentrations, and it is speculated that GOM may have additional sources during

325   this period.

326   Compared with other Hg monitoring in previous studies, some diurnal variation trends of Hg at the

327   SET site were unique. In previous studies (Sprovieri et al., 2016;Yin et al., 2018;Zhang et al.,

328   2015a;Zhang et al., 2016;Fu et al., 2012;Fu et al., 2010;Lan et al., 2012), a common pattern of highest

329   concentration around noon and lowest concentration before sunrise was mostly observed. The decrease

330   in GEM concentration at night may be due to the chemical dissipation of GEM within the stable nocturnal

331   boundary layer, or deposition in the effect of dew (Mao et al., 2008;Kim, 2010). After sunrise, partial

332   GEM re-emission occurs in the sunlight, along with the mixing effect of the residual boundary layer

333   downward, which may lead to an increase in GEM concentration (Mao and Talbot, 2012;Selin et al.,

334   2007;Weiss-Penzias et al., 2009;Talbot et al., 2005). The height of the boundary layer increases after

335   noon during the daytime, which produces dilution of GEM at the surface and may be the reason for the

336   decrease in GEM concentration in the afternoon. The GEM diurnal variation pattern at the SET is

337   particularly special during the PISM period, while a similar variation pattern was also observed at the

338   Qomolangma site in our previous research (Lin et al., 2019), which is another high-altitude site with a

339   sparse population and rare industry. This similar pattern suggests that they have a similar mechanism of

340   GEM diurnal variation. Considering that neither site has an obvious local source of GEM, the variation

341   in GEM concentrations may only be subject to these mechanisms. Similar to the study of Qomolangma,

342   the variation in the boundary layer height may be one of the reasons for the diurnal variation of GEM

343   concentration in the SET region. The stable and low height nocturnal boundary layer at night causes the

344   GEM concentration to gradually concentrate, and the boundary layer gradually increases to a higher

345   altitude after sunrise. The gradual increase in GEM concentration during the daytime may be due to the

346   reduction of GOM from nearby local snowy mountains (Holmes et al., 2010) or the field GEM source

347   brought in by airflow (Lin et al., 2019). During the ISM period, the nighttime GEM dissipation may be

348   due to the fact that this area enters a rapid leaf-growing season (Fu et al., 2016) after entering the ISM

349   period, that the air masses from the Indian Ocean bring a large amount of halogens, and that depletion of

350   GEM occurs under the boundary layer at night.

351   **3.3 Source identification for atmospheric Hg in Nyingchi**

352   To further investigate the contributions of different sources to the SET site, air mass back trajectory

353   simulation and trajectory cluster analyses were performed. Figure 5 shows the cluster analysis results for

354   the PISM and ISM1-3 periods. Based on the results of the total spatial variation index, 3-5 clusters were

355   grouped for each period. Each clustered trajectory contained detailed information about the trajectory

356   from the source region to the SET site, the trajectory frequency during the period, and the concentrations

357   of the pollutants carried by the air mass when the trajectory arrives.

358   During the PISM period (Figure 5a, Table S2), the trajectories mainly originated from or passed

359 through Nepal, northeastern India, and central Tibet, and moved along the southern border of the
360 Himalayas Mountains. During this period, Nyingchi was mainly controlled by westerly circulation. The
361 two clusters with the highest concentrations (traj1 and traj2, with GEM concentrations at 1.21 and 1.20
362 ng m^{-3}) originated from or passed through central Tibet, accounting for 35.32% of all trajectories in this
363 period. Although the GEM concentrations of the two clusters were relatively high during this period, they
364 were still lower than the background GEM concentration in the Northern Hemisphere (~ 1.5-1.7 ng m^{-3}),
365 indicating that the air mass transported to SET station is relative clean. Traj0, from the southern border
366 of the Himalayas, was relatively high in proportion (with a frequency of 61.28%), mainly controlled by
367 the southern branch of the westerly circulation, and has a relatively low concentration (1.05 m^{-3}). This
368 cluster made a turn in the Bay of Bengal and began to ascend toward the Tibetan Plateau, according to
369 UNEP reports (UNEP, 2018;UNEP, 2013b), Hg emission intensities along the trajectory paths were weak.
370 In addition, the air mass arriving at the SET site during this period came from the interior of the continents
371 and contained less water vapor, which may lead to less precipitation and less Hg deposition during the
372 transboundary transport.

373   During the ISM period (Figure 5b-d), the trajectory of arrivals at the SET site changed significantly
374 with the onset and rise of the Indian monsoon. The trajectory path gradually shifted from the southern
375 margin of the Himalayas to the Bay of Bengal. As the source of the air mass changes and the monsoon
376 enters the plateau, it is possible that the concentration of pollutants decreases because of the change in
377 the source region. Because the air mass originated from the Indian Ocean, the concentration of water
378 vapor should increase significantly. During the ISM1 period (Figure 5b, Table S2), both the rising
379 monsoon and the tail of the westerly circulation control the region, causing the transported air masses to
380 exhibit complex trajectories and combined effects. The cluster with the highest concentration (traj2, 0.96
381 ng m^{-3}, and 29.0%) mainly came from or passed through central India. The trajectory with the largest
382 proportion (traj0, 61.45%) had a relatively short path, mainly from northwest India and northern Bay of
383 Bengal, and showed relatively lower concentrations (0.88 m^{-3}). Based on the existing atmospheric Hg
384 emission inventories (Simone et al., 2016;UNEP, 2018;UNEP, 2013b), the Hg emission intensities of
385 northwest India and the Bay of Bengal are very low, which may be the reason for the low GEM
386 concentrations in this cluster. It is noteworthy that although the concentrations were low throughout the
387 period, the trajectories of the different sources showed large concentration differences. Figure S2 shows
388 all the trajectories during the ISM1 period and the GEM concentrations they represent. GEM
389 concentrations are still high in trajectories originating from or passing through northern India and Nepal,
390 which may be related to the high intensities of Hg emissions from anthropogenic sources in those regions
391 (De Simone et al., 2015) and wildfire events (Lin et al., 2019;Finley et al., 2009). Trajectories from
392 central Tibet also have high concentrations, which may be caused by local emissions such as yak dung
393 burning (Lin et al., 2019;Huang et al., 2016), and the local sources do not pass through the areas with
394 high deposition.

395   During the ISM2 period (Figure 5c, Table S2), a typical period of Indian monsoon control, almost
396 all trajectories came from or passed through the southern part of the SET site and were influenced by the
397 monsoon. Only about 5.4% of the trajectories originated from central Tibet with very low GEM
398 concentration (traj0 with 0.81 ng m^{-3} and 3.17%, traj4 with 1.00 ng m^{-3} and 2.24%). Other trajectories

399   were almost identical, but with different track lengths, and showed low GEM concentrations (traj1 with

400   0.90 ng m^{-3} and 70.34%, traj2 0.94 ng m^{-3} and 19.40%). During this period, trajectories that originated

401   in the Indian Ocean brought a large amount of water vapor and caused considerable precipitation during

402   transportation. The Hg carried in the air masses may have been heavily deposited during transport. At

403   the same time, the areas through which the trajectory passed were sparsely populated and underdeveloped

404   and were unable replenish Hg to the air masses. The range of atmospheric mercury concentrations during

405   the ISM2 phase was extremely small (Figure 2), which may indicate that under the strong control of the

406   Indian monsoon, the main source region, transport path, and mechanism of transportation during this

407   period remain stable. Compared with the ISM1 period, although many wildfires existed during this period,

408   the large amount of precipitation may have prevented the dispersion of these pollutants from the wildfire

409   sites.

410   During the ISM3 period (Figure 5d, Table S2), the Indian monsoon remained controlling this region,

411   but its intensity weakened, and the precipitation in the Nyingchi area was greatly reduced. Most of the

412   trajectories still came from northwest India (traj0 and traj3, 46.2% and 45.11%, respectively), and the

413   trajectories remained short. But the GEM concentration at SET increased compared with the ISM1-2

414   period (average at 0.92 ng m^{-3} in ISM1 and ISM2 to 1.04 ng m^{-3} in ISM3 period). At the end of the ISM3

415   period, the GEM concentration showed an upward trend (Figure 2), which may be due to the weakening

416   of monsoon control. A shortened trajectory at the end of the monsoon period was also observed in another

417   study at a nearby site (QNNP) (Lin et al., 2019), which may indicate the withdrawal of the monsoon.

418   To visualize the potential Hg source areas during the monitoring period, PSCF simulation was also

419   applied in this study in combination with the backward trajectories and detailed Hg monitoring at the

420   SET station. Figure 6 shows the potential source regions of Hg during the PISM and ISM periods. The

421   potential source areas of Hg did not change significantly throughout the study period and were mainly

422   concentrated in the YZB Grand Canyon and the southern plains of the Canyon, south of Nyingchi. Due

423   to the complex terrain, even the strong Indian monsoon can linger in the canyon for a long time because

424   of the elevation rise and tortuous path. It is worth noting that heavy precipitation began when the

425   monsoon began to climb and continued until the end of climbing. Therefore, before arriving at the SET

426   station, Hg underwent multiple deposition processes. This may be the reason for the extremely low Hg

427   concentration at the SET station during the monsoon period.

428   **3.4 Hg concentration controlling factor indicated by PCA results in Nyingchi**

429   Overall, 4-5 factors were resolved for each period from the PISM to ISM3 periods. Some factors

430   are unique to each period, and certain factors are found throughout the monitoring period. Table 2 lists

431   the four underlying PCA factors for important Hg-related components. They were assigned as long-

432   distance transport, local emissions, meteorological factor, and snow melt factor.

433   The long-distance transmission factor (F1) found in the PISM and ISM3 periods mainly contain

434   GEM, wind speed, CO (positive loading), temperature, and SO$_2$ (negative). GEM could be considered

435   an indicator of long-distance transportation due to its long lifetime in the atmosphere, especially when

436   GOM and PBM are not significant in this factor. This factor indicates that the long-distance transportation

437   of GEM may mainly occurs in the pre-monsoon and the end of the monsoon period, which is similar to

438   the trajectory analysis in Section 3.3. The negative correlation between GEM and temperature may

439 indicate that the long-distance transport of GEM during the PISM period occurs mainly during periods
440 of lower temperatures. Compared with the diurnal variation of GEM during the ISM period (Figure 4),
441 it is possible that the increasing GEM concentration in the evening in the PISM period is mainly due to
442 the long-distance transportation of GEM.

443   Factor 2 involved GOM and PBM (high positive loading) in each period, mainly with positive O_3,
444 PM_{10}, $PM_{2.5}$, and negative temperature. GOM concentrations were positively correlated with PBM
445 concentrations, which implies that these two species probably originated from the same sources. The
446 high positive loadings of PBM, GOM, and some particle pollutants may indicate that the main source of
447 PBM and GOM is local emissions. The long-distance transport of particle pollutants from the Indian
448 subcontinent may have heavy wet deposition when the air mass climbs into the Tibetan Plateau and
449 cannot reach Nyingchi successfully. Thus, the local monitored particle pollutants, as well as easy-
450 deposition pollutants, may mainly originate from regional emissions. One possible source is from yak
451 dung; in the Tibetan Plateau, yak dung is a widely used household biofuel (Xiao et al., 2015) and the
452 burning of yak dung may release Hg and other particulate matter.

453   Meteorology factor (F3) was found during the ISM period with positive temperature, wind speed,
454 solar radiation, and negative humidity and rain, which are likely associated with meteorological
455 conditions. This factor shows that meteorological conditions may profoundly affect the overall local
456 pollutant distributions during the ISM period, which suggests that the air mass carried by the ISM not
457 only cannot increase the long-distance transportation of pollutants to the Nyingchi area, but may also
458 reduce the local contribution of pollution. For existing pollutants, the strong positive loading of solar
459 radiation may indicate that pollutant reactions under strong radiation are relatively active in this high-
460 altitude region. The strong negative humidity and rain may indicate that rain has played a strong role in
461 the cleaning process, especially during the ISM1 and ISM2 periods, when precipitation is relatively
462 strong.

463   Factor 4 had a strong positive correlation with GEM, ROM, and solar radiation, and negative loading
464 with humidity during the ISM1 period. This suggests that as solar radiation increases in the afternoon
465 (Figure 3), more GEM and GOM are emitted to the air, which may reflect the snow/ice melt process
466 (Huang et al., 2010;Dommergue et al., 2003). Previous studies have shown that the snowmelt process
467 can increase atmospheric GEM concentration (Huang et al., 2010;Dommergue et al., 2003). GEM may
468 come from the evaporation of snow melting or be driven by the photoreduction of snow Hg^{II} (Song et al.,
469 2018). Previous simulations indicated that the oxidation of GEM may occur at the snow/ice interface in
470 the action of solar radiation, leading to extra GOM release in the ISM1 period. The peak concentrations
471 of GEM and GOM both appeared in the afternoon during the ISM1 period, when the solar radiation was
472 the highest and humidity was the lowest. The increase in GEM and GOM concentrations may be related
473 to solar radiation, according to the PCA results.

474 **3.5 Implications**

475   The Tibetan Plateau is a direct invasion target of the ISM. Blocked by the high altitude of the
476 Himalayas, the Indian monsoon could bypass the high mountains and enter Tibet via the YZB Grand
477 Canyon. When the summer monsoon enters Tibet, it is generally believed that pollutants from India and
478 the Indian Ocean, as well as large amounts of water vapor, may be carried along with the air masses (Lin

479   et al., 2019;Yang et al., 2013;Wang et al., 2018). Located in the water vapor channel where the Indian

480   monsoon enters, Nyingchi is believed to receive a large amount of foreign air mass (Yang et al., 2013).

481   Considering that Nyingchi has little local emission because of the sparse population and lack of industry,

482   the pollutants present in the area should mostly have been transported by monsoons over long distances.

483   However, our monitoring results show that during the ISM period, the Hg concentrations in the Nyingchi

484   are extremely low (0.95 ± 0.27 ng m^{-3}); lower than the background Hg concentration in the Northern

485   Hemisphere and the Hg concentrations observed at surrounding monitoring sites in the literature (Table

486   1).

487   The low concentration during the ISM period may be related to the regional deposition process and

488   complex regional terrain. When monsoon winds carry large amounts of Indian Ocean moisture and enter

489   the YZB Grand Canyon, strong wet deposition occurs during transport due to an increase in elevation

490   and a decrease in temperature. The process of rainwater scouring from wet deposition may result in

491   significant deposition of pollutants from carried air masses (Lindberg and Stratton, 1998;Seigneur et al.,

492   2006). Meanwhile, the air flow in the canyon is slow owing to the complex terrain. The slow migration

493   of the air mass further strengthens the deposition process. In addition, during the ISM period, the dense

494   forest in the canyon may deplete some of the mercury during transport (Fu et al., 2016). Therefore,

495   pollutants from the Indian subcontinent struggle to go deep into the Tibetan Plateau during the ISM

496   period. The deposited pollutants may flow into the downstream area via rivers to Southeast Asia and

497   South Asia, and these transportation mechanisms needs to be further studied. However, long-distance

498   transboundary transport remains an important mechanism of Hg distribution in this area during the period

499   of westerly circulation. As discussed in Section 3.1, the Hg concentration in Nyingchi during PISM

500   period (1.20 ± 0.35 ng m^{-3}) was much higher than that during the ISM period (0.95 ± 0.27 ng m^{-3}). The high

501   Hg concentration during the PISM period may indicate that a large amount of external source Hg entered

502   the Nyingchi area during the non-ISM period, which needs to be further studied.

503   The results of our previous study on Qomolangma were different from those in Nyingchi. At

504   Qomolangma(Lin et al., 2019), the ISM was the main period of transboundary transport of Hg, and the

505   PISM period accounted for a smaller amount of transport. The difference in Hg transportation patterns

506   between the two sites may mainly originate from the difference in the geographical location, with

507   different actions of the westerly circulation and the Indian summer wind. Qomolangma is located on the

508   northern side of the Himalayas, a typical terrain on the southern side of the Tibetan Plateau. The Nyingchi

509   area is another typical pathway for air masses to enter the Tibetan Plateau. Together, they describe two

510   typical transboundary transport patterns of Hg occurring on the Tibetan Plateau at different periods of

511   the year.

512   **4. Conclusions**

513   Comprehensive species Hg monitoring was carried out in Nyingchi, a high-altitude site in the

514   southeast of the Tibetan Plateau. Nyingchi is located on the main pathway for water vapor carried by the

515   monsoon to enter Tibet during the ISM period, which could characterize the spread of pollutants from

516   the Indian subcontinent. The atmospheric Hg concentrations during the PISM period (1.20 ± 0.35 ng m^{-3},

517   13.5 ± 7.3 pg m^{-3}, and 11.4 ± 4.8 pg m^{-3}, for GEM, GOM, and PBM respectively) were relatively higher

518   than those during the ISM period (0.95 ± 0.21 ng m^{-3}, 12.7 ± 14.3 pg m^{-3}, and 8.8 ± 6.0 pg m^{-3}, for GEM,

GOM, and PBM respectively). The Hg concentration in Nyingchi is particularly low compared with other high-altitude stations around the world. GEM concentration shows a distinct and unique diurnal variation, with a gradual increase in GEM concentration during the day and a maximum concentration at night. This diurnal variation may be due to the re-emission of GEM by snowmelt and the trapping effect of pollutants by the planetary boundary layer at night.

According to the trajectory model, atmospheric Hg in the Nyingchi area originated mainly from or passed through Nepal and central Tibet during the PISM period. During the ISM period, Hg may mainly originate from northeast India and the Bay of Bengal. During the ISM period, the Hg concentrations were particularly low because of the strong deposition process during transportation. Through comprehensive PCA analysis using local meteorological conditions and multiple pollutants, long-distance transport, local emissions, meteorological factor, and snowmelt factor have been identified to affect local Hg concentrations. In the Nyingchi area, Hg mainly comes from westerly circulation during the non-ISM period. During the ISM period, pollutants from the Indian subcontinent may travel to South Asia and Southeast Asia along the major rivers in this area.

Acknowledgments

This study was funded by the National Natural Science Foundation of China (Grant #41630748, 41977311, 41977324, 41821005). The authors are grateful to NOAA for providing the HYSPLIT model and GFS meteorological files. We also thank the staffs of the South-East Tibetan Plateau Station for Integrated Observation and Research of Alpine Environment, Chinese Academy of Sciences on Nyingchi for field sampling assistance.

Data availability. All the data presented in this paper can be made available for scientific purposes upon request to the corresponding authors.

Author contributions. HL,XW, YT, QZ and XY designed the research and performed field measurements. HL YT and CY performed the data analysis and model simulations. HL led the paper writing. LC,SK,LL,JS and BF contributed to the scientific discussion and the paper preparation.

Competing interests. The authors declare that they have no conflict of interest.

Figure captions

Figure 1. Location of the South-East Tibetan Plateau Station for Integrated Observation and Research of Alpine Environment (SET station or Nyingchi station, the red star). SET station is located in a water vapor channel from the Ganges River Plain to the Tibetan Plateau. The red dot is Lhasa, the capital city of the Tibet Autonomous Region, which is the most densely populated city in Tibet; the other red dot is the nearest town to the monitoring site, Bayi Town.

Figure 2. Time serious of GEM, GOM, and PBM concentrations and the daily rainfall over the

558 sampling period. The GEM concentration resolution is 5 min, and the GOM, PBM, and rain

559 resolutions are 2 hours. According to the characters of monsoon development and precipitation, the

560 monitoring periods are divided into four segments, namely PISM (before May), ISM1 (1 May- 2

561 June), ISM2 (3 June – 8 August), and ISM3 (after 9 August).

562 Figure 3. GEM concentrations obtained through passive samplers throughout the year. The black

563 squares represent the atmospheric Hg concentrations obtained by passive sampling, and the upper

564 and lower error lines are the standard errors of the passive samples monitored during the same time

565 period. The red dots represent the GEM concentrations obtained through the Tekran instrument. The

566 green horizontal line indicates the average of the atmospheric mercury concentrations during this

567 period.

568 Figure 4. Diurnal variation of species Hg, concentrations of some other pollutants and

569 meteorological information from PISM to ISM1-3 periods. The short horizontal line represents the

570 concentration error range for each time period.

571 Figure 5. Clusters of the back trajectory analysis from SET site during PISM to ISM3 periods. The

572 thickness of the line represents the ratio of the cluster in the time period, and the color of the line

573 represents the GEM concentration carried by the cluster, the background is the globally Hg emission

574 inventory developed by UNEP(UNEP, 2013a).

575 Figure 6. Potential source regions and pathways for the results of PSCF analysis. The PSCF values

576 represent the probability that a grid cell is a source of Hg. (From a-d are PISM, ISM1-3 periods

577 respectively)

578 **Table captions**

579 Table 1. Comparison of atmospheric Hg concentrations at high elevation (> 2000 m a.s.l) stations

580 Table 2. PCA factor loadings (Varimax Rotated Factor Matrix) for Hg in Nyingchi, Tibet, China

581

582

583 Figure 1
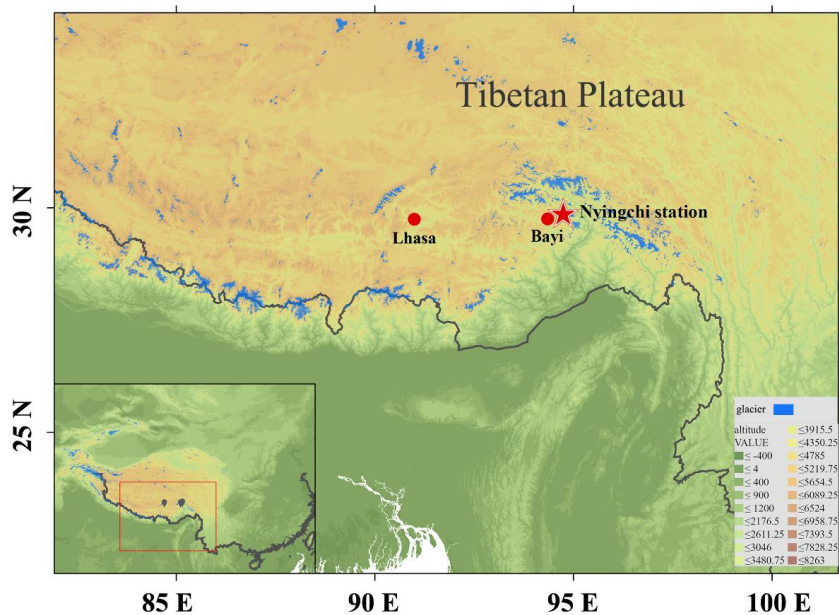
584
585

586

587   Figure 2
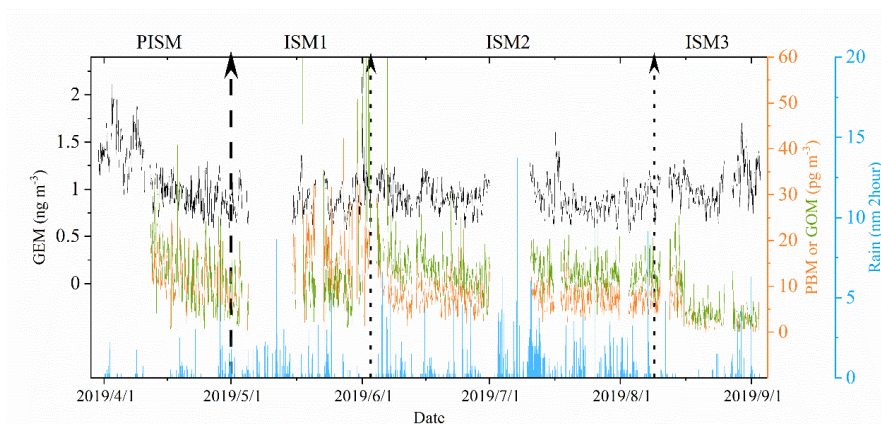
588
589

590   Figure 3
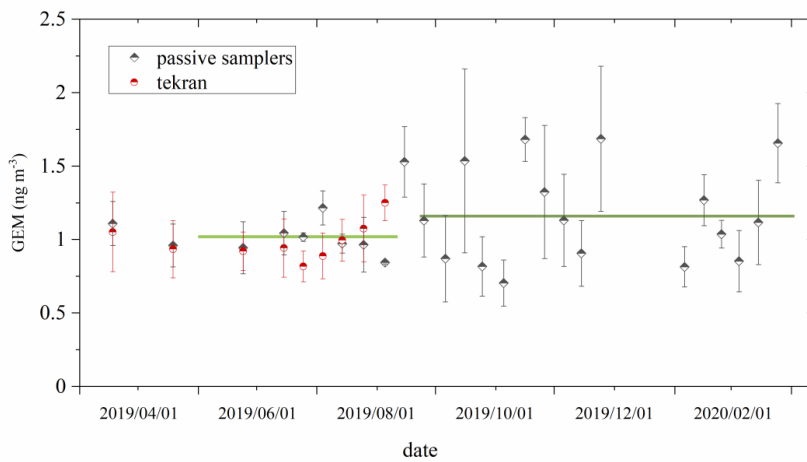
591
592

593

594   Figure 4
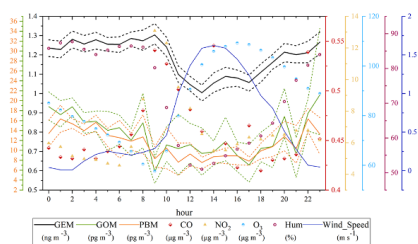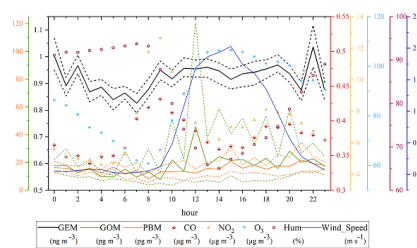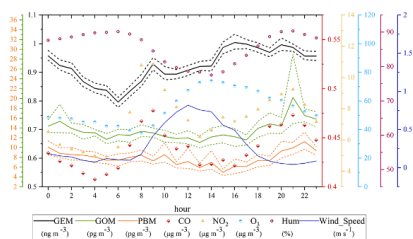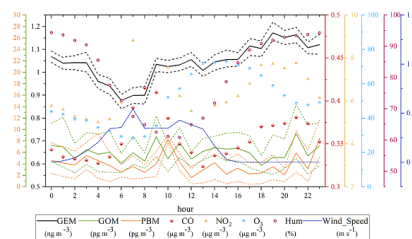
595
596

597

598   Figure 5

599   a.
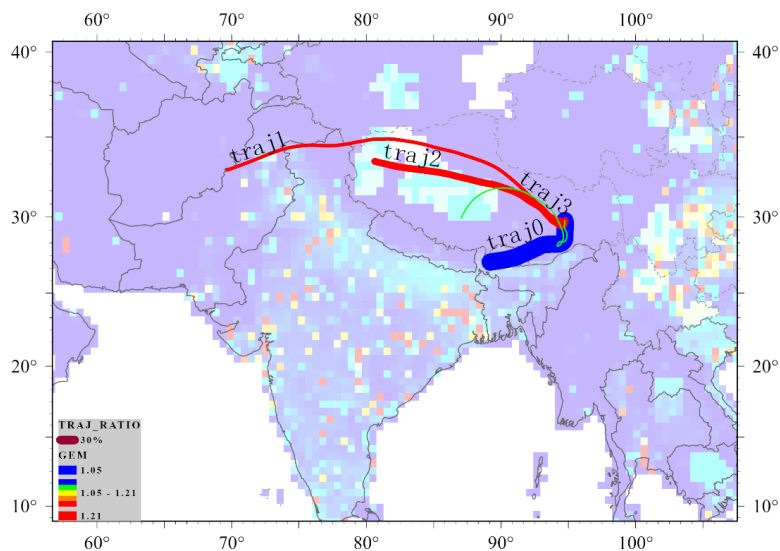
600
601
602

603   b.
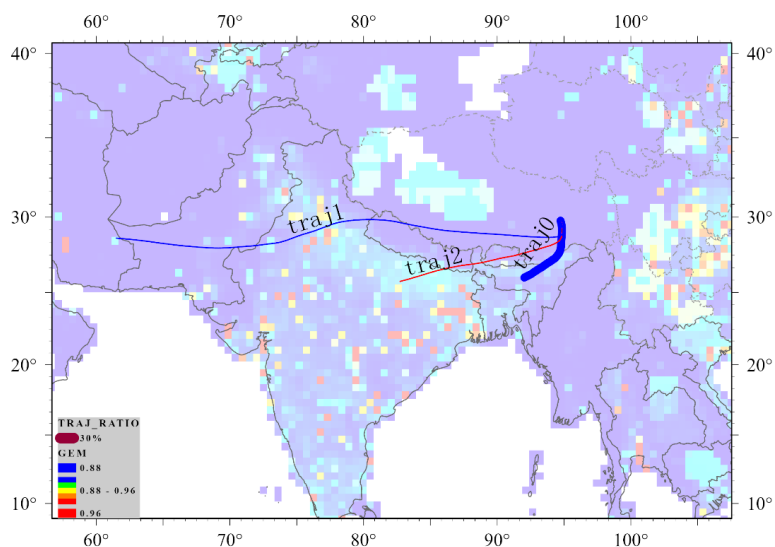
604
605
606

607   c.
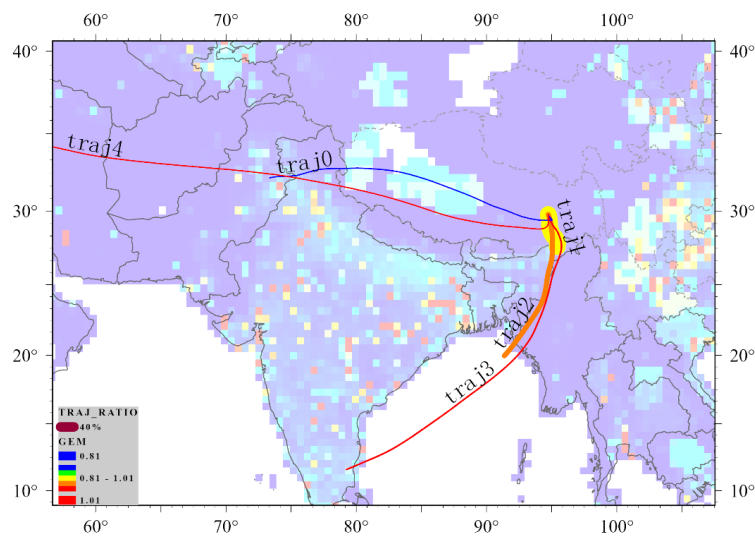
608
609
610

611   d.
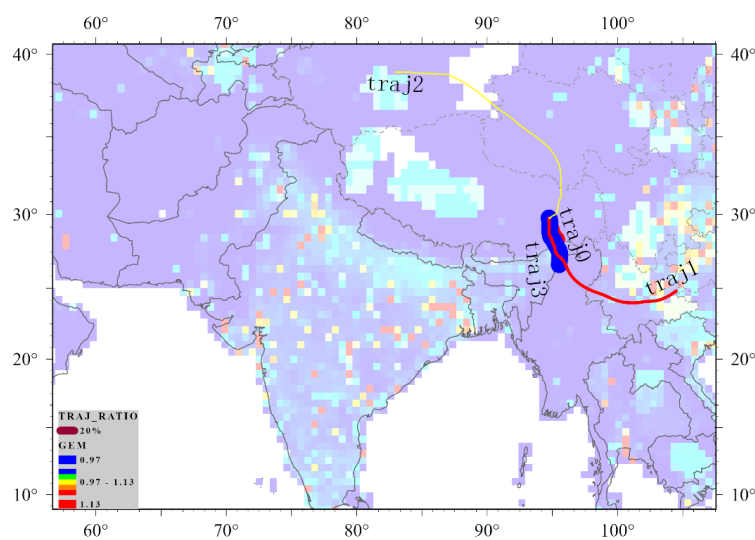
612
613

614   Figure 6

615
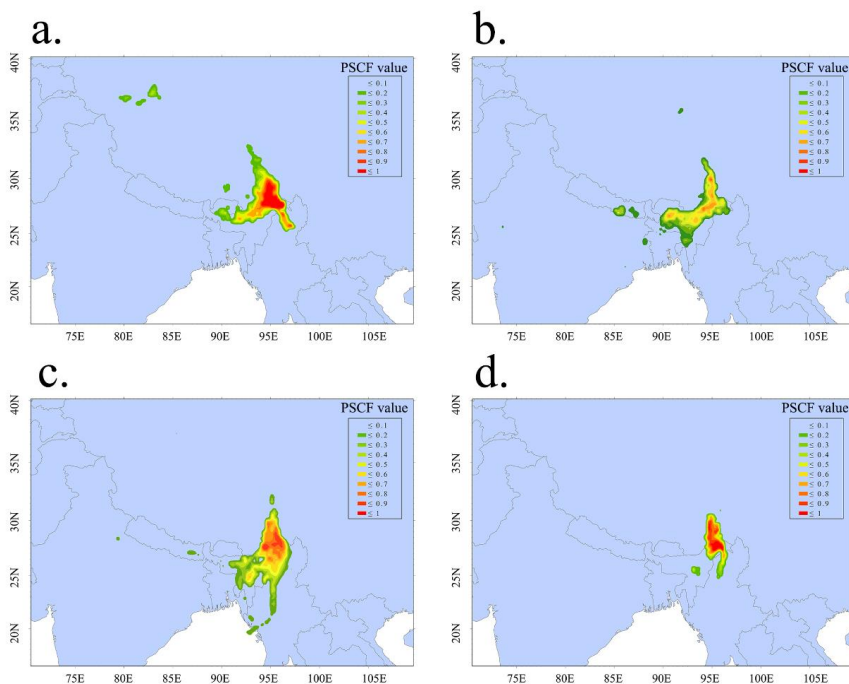
616

617

Table 1. Comparison of atmospheric Hg concentrations at high elevation (>2000m a.s.l) stations

Site	Country	Lat & Lon	Elevation	Type	Time Period	GEM or TGM mean±SD, ng/m3	GOM mean±SD, pg/m3	PBM mean±SD, pg/m3	Reference
Concordia Station	Antarctica	-79.1/123.35	3220	Remote	2013-2014	0.80±0.25	-	-	Sprovieri et al., 2016
SET	**China**	**29.77/94.74**	**3263**	**Remote**	**2019**	**1.01±0.27**	**12.8±13.3**	**9.3±5.9**	**This study**
Ev-K2	Nepal	27.96/86.81	5050	Remote	2012-2014	1.19±0.30	-	-	Sprovieri et al., 2016
Nam Co	China	30.78/90.99	4730	Remote	2012-2014	1.33 ±0.24	-	-	Yin et al., 2018
Qomolangma	China	28.37/86.95	4276	Remote	2016	1.42±0.37	21.4±13.4	25.6±19.1	Lin et al.,2016
Kodaicanal	India	10.23/77.47	2333	Rural	2013-2014	1.54±0.23	-	-	Sprovieri et al., 2016
Col Margherita	Italy	46.37/11.79	2545	Rural	2014	1.69±0.29	-	-	Sprovieri et al., 2016
Lulin	China	23.51/120.92	2862	Remote	2006-2007	1.73±0.61	12.1±20.0	2.3±3.9	Sheu et al., 2010
Mt. Walinguan	China	36.29/100.90	3816	Remote	2007-2008	1.98±0.98	7.4±4.8	19.4±18.0	Fu et al., 2012c
Mt.Ailao	China	24.53/101.02	2450	Remote	2011-2012	2.09±0.63	2.2±2.3	31.3±28.0	Zhang et al., 2016
Shangri-La	China	28.02/99.73	3580	Rural	2009-2010	2.55±0.73	8.2±7.9	38.8±31.3	Zhang et al., 2015
Mt. Leigong	China	26.39/108.20	2178	Remote	2008-2009	2.8±1.51	-	-	Fu et al., 2010b

Table 2. PCA Factor Loadings (Varimax Rotated Factor Matrix) for Hg in Nyingchi, Tibet, China

tentative identification		GEM	PBM	GOM	Temp	Hum	Wind_Speed	Rain	Solar_Rad	CO	NO₂	O₃	PM₁₀	PM₂.₅	SO₂	VE
long-distance transport	PISM	**0.92**		0.10	**-0.79**		**0.64**	-0.15		0.28	0.43			-0.27	**-0.73**	19.86
	ISM3	**0.78**			-0.22	0.26	0.18	0.49	-0.13	**0.76**		0.29	-0.11		**-0.83**	17.05
local emission	PISM	0.13	**0.91**	**0.92**			-0.20			0.22	-0.47	-0.13	0.12		-0.44	15.96
	ISM1	0.26	**0.56**	0.19				-0.12	-0.16		-0.12		**0.69**	**0.86**	0.32	12.97
	ISM1	0.17	**0.60**	0.16	-0.40		0.19	-0.14	-0.11			**0.91**	0.22	-0.19		11.11
	ISM2	0.50	**0.89**	**0.77**	**-0.51**	-0.52	**0.71**	-0.12	0.10	0.14		**0.71**	**0.71**	**0.72**		30.26
	ISM3	0.25	**0.96**	**0.95**	-0.13	-0.19	-0.12	-0.34	0.27			-0.15		0.16	0.32	16.46
meteorology	ISM1		-0.18	0.11	**0.82**	**-0.77**	**0.62**	**-0.80**	**0.68**		**-0.59**		0.13		0.31	23.46
	ISM2	**-0.51**		-0.23	**0.66**	**-0.80**	0.21	**-0.79**	**0.85**		-0.10	0.25	0.43	0.18	-0.13	22.02
	ISM3	-0.19	0.17		**0.85**	**-0.89**		-0.30	**0.88**	-0.44		0.46	0.31	0.21		21.49
melt	ISM1	**0.78**	0.13	**0.85**		**-0.57**			**0.50**		0.33	0.24	0.21	0.21	0.25	15.94

629

Reference

631 Ambrose, J. L.: Improved methods for signal processing in measurements of mercury by Tekran®
632 2537A and 2537B instruments, Atmospheric Measurement Techniques, 10, 5063-5073, 2017.
633 Ashbaugh, L. L., Malm, W. C., and Sadeh, W. Z.: A residence time probability analysis of sulfur
634 concentrations at Grand Canyon National Park, Atmospheric Environment (1967), 19, 1263-1270,
635 1985.
636 Brooks, S., Luke, W., Cohen, M., Kelly, P., Lefer, B., and Rappenglück, B. J. A. E.: Mercury species
637 measured atop the Moody Tower TRAMP site, Houston, Texas, 44, 4045-4055, 2010.
638 Chai, T., Stein, A., Ngan, F., and Draxler, R.: Inverse modeling with HYSPLIT Lagrangian Dispersion
639 Model-Tests and Evaluation using the Cross Appalachian Tracer Experiment (CAPTEX) data, AGU
640 Fall Meeting Abstracts, 2016.
641 Chai, T., Crawford, A., Stunder, B., Pavolonis, M. J., Draxler, R., and Stein, A.: Improving volcanic ash
642 predictions with the HYSPLIT dispersion model by assimilating MODIS satellite retrievals,
643 Atmospheric Chemistry and Physics, 17, 2865-2879, 2017.
644 Chen, G., Li, J., Chen, B., Wen, C., Yang, Q., Alsaedi, A., and Hayat, T.: An overview of mercury
645 emissions by global fuel combustion: the impact of international trade, Renewable and Sustainable
646 Energy Reviews, 65, 345-355, 2016.
647 Cheng, I., Zhang, L., Blanchard, P., Graydon, J., St Louis, V. J. A. C., and Physics: Source-receptor
648 relationships for speciated atmospheric mercury at the remote Experimental Lakes Area,
649 northwestern Ontario, Canada, 12, 1903-1922, 2012.
650 de Foy, B., Tong, Y., Yin, X., Zhang, W., Kang, S., Zhang, Q., Zhang, G., Wang, X., and Schauer, J. J.:
651 First field-based atmospheric observation of the reduction of reactive mercury driven by sunlight,
652 Atmospheric Environment, 134, 7e39, 2016.
653 De Simone, F., Cinnirella, S., Gencarelli, C. N., Yang, X., Hedgecock, I. M., and Pirrone, N.: Model
654 study of global mercury deposition from biomass burning, Environmental science & technology,
655 49, 6712-6721, 2015.
656 Dommergue, A., Ferrari, C. P., Gauchard, P. A., Boutron, C. F., Poissant, L., Pilote, M., Jitaru, P., and
657 Adams, F. C. J. G. r. l.: The fate of mercury species in a sub-arctic snowpack during snowmelt, 30,
658 2003.
659 Feng, L., and Zhou, T. J. J. o. G. R. A.: Water vapor transport for summer precipitation over the
660 Tibetan Plateau: Multidata set analysis, 117, 2012.
661 Feng, Y., Wang, W., and Liu, J. J. W.: Dilemmas in and Pathways to Transboundary Water
662 Cooperation between China and India on the Yaluzangbu-Brahmaputra River, 11, 2096, 2019.
663 Finley, B., Swartzendruber, P., and Jaffe, D.: Particulate mercury emissions in regional wildfire
664 plumes observed at the Mount Bachelor Observatory, Atmospheric Environment, 43, 6074-6083,
665 2009.
666 Fu, X., Feng, X., Dong, Z., Yin, R., Wang, J., Yang, Z., and Zhang, H.: Atmospheric gaseous elemental
667 mercury (GEM) concentrations and mercury depositions at a high-altitude mountain peak in south
668 China, Atmospheric Chemistry and Physics, 10, 2425-2437, 2010.
669 Fu, X., Feng, X., Liang, P., Zhang, H., Ji, J., and Liu, P.: Temporal trend and sources of speciated
670 atmospheric mercury at Waliguan GAW station, Northwestern China, Atmospheric Chemistry and
671 Physics, 12, 1951-1964, 2012.
672 Fu, X., Zhu, W., Zhang, H., Sommar, J., Yu, B., Yang, X., Wang, X., Lin, C.-J., and Feng, X.: Depletion
673 of atmospheric gaseous elemental mercury by plant uptake at Mt. Changbai, Northeast China,
674 Atmospheric Chemistry and Physics, 16, 12861-12873, 2016.
675 Gay, D. A., Schmeltz, D., Prestbo, E., Olson, M., Sharac, T., and Tordon, R.: The Atmospheric Mercury
676 Network: measurement and initial examination of an ongoing atmospheric mercury record across
677 North America, Atmospheric Chemistry and Physics, 13, 11339-11349, 10.5194/acp-13-11339-

678 2013, 2013.

679 Gong, P., Wang, X., Pokhrel, B., Wang, H., Liu, X., Liu, X., Wania, F. J. E. s., and technology: Trans-
680 Himalayan Transport of Organochlorine Compounds: Three-Year Observations and Model-Based
681 Flux Estimation, 53, 6773-6783, 2019a.

682 Gong, S., Hagan, D. F., and Zhang, C. J. J. o. S.: Analysis on Precipitable Water Vapor over the
683 Tibetan Plateau Using FengYun-3A Medium Resolution Spectral Imager Products, 2019, 2019b.

684 Guo, H., Lin, H., Zhang, W., Deng, C., Wang, H., Zhang, Q., Shen, Y., and Wang, X.: Influence of
685 meteorological factors on the atmospheric mercury measurement by a novel passive sampler,
686 Atmospheric Environment, 97, 310-315, 10.1016/j.atmosenv.2014.08.028, 2014.

687 Gustin, M. S., Amos, H. M., Huang, J., Miller, M. B., and Heidecorn, K.: Measuring and modeling
688 mercury in the atmosphere: a critical review, Atmospheric Chemistry and Physics, 15, 5697-5713,
689 2015.

690 Holmes, C. D., Jacob, D. J., Corbitt, E. S., Mao, J., Yang, X., Talbot, R., and Slemr, F.: Global
691 atmospheric model for mercury including oxidation by bromine atoms, Atmospheric Chemistry
692 and Physics, 10, 12037-12057, 2010.

693 Hopke, P. K. J. J. o. t. A., and Association, W. M.: Review of receptor modeling methods for source
694 apportionment, 66, 237-259, 2016.

695 Horowitz, H. M., Jacob, D. J., Zhang, Y., Dibble, T. S., Slemr, F., Amos, H. M., Schmidt, J. A., Corbitt,
696 E. S., Marais, E. A., and Sunderland, E. M.: A new mechanism for atmospheric mercury redox
697 chemistry: Implications for the global mercury budget, Atmospheric Chemistry and Physics, 17,
698 6353-6371, 2017.

699 Huang, J., Choi, H.-D., Hopke, P. K., Holsen, T. M. J. E. s., and technology: Ambient mercury sources
700 in Rochester, NY: results from principle components analysis (PCA) of mercury monitoring network
701 data, 44, 8441-8445, 2010.

702 Huang, J., Kang, S., Zhang, Q., Guo, J., Sillanpää, M., Wang, Y., Sun, S., Sun, X., and Tripathee, L.:
703 Characterizations of wet mercury deposition on a remote high-elevation site in the southeastern
704 Tibetan Plateau, Environmental Pollution, 206, 518-526, 2015.

705 Huang, J., Kang, S., Guo, J., Zhang, Q., Cong, Z., Sillanpää, M., Zhang, G., Sun, S., and Tripathee, L.:
706 Atmospheric particulate mercury in Lhasa city, Tibetan Plateau, Atmospheric Environment, 142,
707 433-441, 2016.

708 Hurst, T., and Davis, C.: Forecasting volcanic ash deposition using HYSPLIT, Journal of Applied
709 Volcanology, 6, 5, 2017.

710 Jackson, J. E.: A user's guide to principal components, John Wiley & Sons, 2005.

711 Jiang, X., and Wang, F.: Mercury emissions in China: a general review, Waste Disposal & Sustainable
712 Energy, 1, 127-132, 2019.

713 Kellerhals, M., Beauchamp, S., Belzer, W., Blanchard, P., Froude, F., Harvey, B., McDonald, K., Pilote,
714 M., Poissant, L., and Puckett, K.: Temporal and spatial variability of total gaseous mercury in Canada:
715 results from the Canadian Atmospheric Mercury Measurement Network (CAMNet), Atmospheric
716 Environment, 37, 1003-1011, 2003.

717 Kim, S. Y.: Continental outflow of polluted air from the US to the North Atlantic and mercury
718 chemical cycling in various atmospheric environments, 2010.

719 Lan, X., Talbot, R., Castro, M., Perry, K., and Luke, W.: Seasonal and diurnal variations of atmospheric
720 mercury across the US determined from AMNet monitoring data, Atmospheric Chemistry and
721 Physics, 12, 10569-10582, 2012.

722 Landis, M. S., Stevens, R. K., Schaedlich, F., and Prestbo, E. M.: Development and characterization
723 of an annular denuder methodology for the measurement of divalent inorganic reactive gaseous
724 mercury in ambient air, Environmental science & technology, 36, 3000-3009, 2002.

725 Li, C., Bosch, C., Kang, S., Andersson, A., Chen, P., Zhang, Q., Cong, Z., Chen, B., Qin, D., and
726 Gustafsson, Ö.: Sources of black carbon to the Himalayan–Tibetan Plateau glaciers, Nature
727 Communications, 7, 12574, 2016.

728 Lin, H., Zhang, W., Deng, C., Tong, Y., Zhang, Q., Wang, X. J. E. S., and Research, P.: Evaluation of

729 passive sampling of gaseous mercury using different sorbing materials, 24, 14190-14197, 2017.

730 Lin, H., Tong, Y., Yin, X., Zhang, Q., Zhang, H., Zhang, H., Long, C., Kang, S., Zhang, W., Schauer, J.
731 J. A. C., and Physics: First measurement of atmospheric mercury species in Qomolangma Natural
732 Nature Preserve, Tibetan Plateau, and evidence oftransboundary pollutant invasion, 19, 1373-1391,
733 2019.

734 Lindberg, S. a., and Stratton, W.: Atmospheric mercury speciation: concentrations and behavior of
735 reactive gaseous mercury in ambient air, Environmental Science & Technology, 32, 49-57, 1998.

736 Liu, B., Keeler, G. J., Dvonch, J. T., Barres, J. A., Lynam, M. M., Marsik, F. J., and Morgan, J. T. J. A. E.:
737 Temporal variability of mercury speciation in urban air, 41, 1911-1923, 2007.

738 Mao, H., Talbot, R., Sigler, J., Sive, B., and Hegarty, J.: Seasonal and diurnal variations of Hg over
739 New England, Atmospheric Chemistry and Physics, 8, 1403-1421, 2008.

740 Mao, H., and Talbot, R.: Speciated mercury at marine, coastal, and inland sites in New England—
741 Part 1: Temporal variability, Atmospheric Chemistry and Physics, 12, 5099-5112, 2012.

742 Ping, C., and Bo, L.: Analysis of water vapor transport characteristics in southeast Tibet and its
743 impact, Southern Agriculture, China, 12, 124-125, 2018.

744 Pokhrel, B., Gong, P., Wang, X., Gao, S., Wang, C., and Yao, T.: Sources and environmental
745 processes of polycyclic aromatic hydrocarbons and mercury along a southern slope of the Central
746 Himalayas, Nepal, Environmental Science and Pollution Research, 23, 13843-13852, 2016.

747 Polissar, A., Hopke, P., Paatero, P., Kaufmann, Y., Hall, D., Bodhaine, B., Dutton, E., and Harris, J.:
748 The aerosol at Barrow, Alaska: long-term trends and source locations, Atmospheric Environment,
749 33, 2441-2458, 1999.

750 Qiu, J.: China: the third pole, Nature News, 454, 393-396, 2008.

751 Rutter, A. P., Schauer, J. J., Lough, G. C., Snyder, D. C., Kolb, C. J., Von Klooster, S., Rudolf, T.,
752 Manolopoulos, H., and Olson, M. L.: A comparison of speciated atmospheric mercury at an urban
753 center and an upwind rural location, Journal of Environmental Monitoring, 10, 102-108, 2008.

754 Seigneur, C., Vijayaraghavan, K., and Lohman, K.: Atmospheric mercury chemistry: Sensitivity of
755 global model simulations to chemical reactions, Journal of Geophysical Research: Atmospheres,
756 111, 2006.

757 Selin, N. E., Jacob, D. J., Park, R. J., Yantosca, R. M., Strode, S., Jaeglé, L., and Jaffe, D.: Chemical
758 cycling and deposition of atmospheric mercury: Global constraints from observations, Journal of
759 Geophysical Research: Atmospheres, 112, 2007.

760 Selin, N. E.: Global biogeochemical cycling of mercury: a review, Annual Review of Environment
761 and Resources, 34, 43, 2009.

762 Sheng, J., Wang, X., Gong, P., Joswiak, D. R., Tian, L., Yao, T., Jones, K. C. J. E. s., and technology:
763 Monsoon-driven transport of organochlorine pesticides and polychlorinated biphenyls to the
764 Tibetan Plateau: three year atmospheric monitoring study, 47, 3199-3208, 2013.

765 Simone, F. D., Gencarelli, C. N., Hedgecock, I. M., and Pirrone, N.: A modeling comparison of
766 mercury deposition from current anthropogenic mercury emission inventories, Environmental
767 science & technology, 50, 5154-5162, 2016.

768 Slemr, F., Weigelt, A., Ebinghaus, R., Kock, H. H., Bödewadt, J., Brenninkmeijer, C. A., Rauthe-Schöch,
769 A., Weber, S., Hermann, M., and Becker, J.: Atmospheric mercury measurements onboard the
770 CARIBIC passenger aircraft, Atmospheric Measurement Techniques, 9, 2291-2302, 2016.

771 Song, S., Angot, H., Selin, N. E., Gallée, H., Sprovieri, F., Pirrone, N., Helmig, D., Savarino, J., Magand,
772 O., and Dommergue, A.: Understanding mercury oxidation and air–snow exchange on the East
773 Antarctic Plateau: a modeling study, 2018.

774 Sprovieri, F., Gratz, L., and Pirrone, N.: Development of a ground-based atmospheric monitoring
775 network for the Global Mercury Observation System (GMOS), E3S Web of Conferences, 2013.

776 Sprovieri, F., Pirrone, N., Bencardino, M., D'Amore, F., Carbone, F., Cinnirella, S., Mannarino, V.,
777 Landis, M., Ebinghaus, R., and Weigelt, A.: Atmospheric mercury concentrations observed at
778 ground-based monitoring sites globally distributed in the framework of the GMOS network,
779 Atmospheric Chemistry and Physics, 16, 11915-11935, 2016.

780 Stein, A., Draxler, R. R., Rolph, G. D., Stunder, B. J., Cohen, M., and Ngan, F.: NOAA's HYSPLIT
781 atmospheric transport and dispersion modeling system, Bulletin of the American Meteorological
782 Society, 96, 2059-2077, 2015.
783 Stylo, M., Alvarez, J., Dittkrist, J., and Jiao, H.: Global review of mercury monitoring networks, UNEP,
784 Geneva, 2016.
785 Swartzendruber, P., Jaffe, D., and Finley, B.: Improved fluorescence peak integration in the Tekran
786 2537 for applications with sub-optimal sample loadings, Atmospheric Environment, 43, 3648-3651,
787 2009.
788 Talbot, R., Mao, H., and Sive, B.: Diurnal characteristics of surface level O3 and other important
789 trace gases in New England, Journal of Geophysical Research: Atmospheres, 110, 2005.
790 Tong, Y., Yin, X., Lin, H., Wang, H., Deng, C., Chen, L., Li, J., Zhang, W., Schauer, J. J., and Kang, S.:
791 Recent Decline of Atmospheric Mercury Recorded by Androsace tapete on the Tibetan Plateau,
792 Environmental science & technology, 50, 13224-13231, 2016.
793 Travnikov, O., Angot, H., Artaxo, P., Bencardino, M., Bieser, J., D'Amore, F., Dastoor, A., Simone, F.
794 D., Diéguez, M. d. C., and Dommergue, A.: Multi-model study of mercury dispersion in the
795 atmosphere: atmospheric processes and model evaluation, Atmospheric Chemistry and Physics,
796 17, 5271-5295, 2017.
797 UNEP: Minamata Convention on Mercury, in, UNEP Geneva, 2013a.
798 UNEP: The Global Mercury Assessment: UN Environment Programme, Chemicals & Health Branch,
799 Geneva, Switzerland (2018), 2018.
800 UNEP, U. G. M. A.: Sources, Emissions, Releases and Environmental Transport; UNEP Chemicals
801 Branch: Geneva, Switzerland, 2013, There is no corresponding record for this reference, 2013b.
802 Wang, C., Wang, X., Gong, P., and Yao, T.: Long-term trends of atmospheric organochlorine
803 pollutants and polycyclic aromatic hydrocarbons over the southeastern Tibetan Plateau, Science
804 of the Total Environment, 624, 241-249, 2018.
805 Wang, X., Gong, P., Sheng, J., Joswiak, D. R., and Yao, T.: Long-range atmospheric transport of
806 particulate Polycyclic Aromatic Hydrocarbons and the incursion of aerosols to the southeast
807 Tibetan Plateau, Atmospheric Environment, 115, 124-131, 2015.
808 Weiss-Penzias, P., Gustin, M. S., and Lyman, S. N.: Observations of speciated atmospheric mercury
809 at three sites in Nevada: Evidence for a free tropospheric source of reactive gaseous mercury,
810 Journal of Geophysical Research: Atmospheres, 114, 2009.
811 Xiao, Q., Saikawa, E., Yokelson, R. J., Chen, P., Li, C., and Kang, S.: Indoor air pollution from burning
812 yak dung as a household fuel in Tibet, Atmospheric Environment, 102, 406-412,
813 10.1016/j.atmosenv.2014.11.060, 2015.
814 Xu, K., Zhong, L., Ma, Y., Zou, M., Huang, Z. J. T., and Climatology, A.: A study on the water vapor
815 transport trend and water vapor source of the Tibetan Plateau, 1-12, 2020.
816 Yang, J., Kang, S., Ji, Z., and Chen, D.: Modeling the origin of anthropogenic black carbon and its
817 climatic effect over the Tibetan Plateau and surrounding regions, Journal of Geophysical Research:
818 Atmospheres, 123, 671-692, 2018.
819 Yang, W., Yao, T., Guo, X., Zhu, M., Li, S., and Kattel, D. B. J. J. o. G. R. A.: Mass balance of a maritime
820 glacier on the southeast Tibetan Plateau and its climatic sensitivity, 118, 9579-9594, 2013.
821 Yin, X., Kang, S., Foy, B. d., Ma, Y., Tong, Y., Zhang, W., Wang, X., Zhang, G., and Zhang, Q.: Multi-
822 year monitoring of atmospheric total gaseous mercury at a remote high-altitude site (Nam Co,
823 4730 m asl) in the inland Tibetan Plateau region, Atmospheric Chemistry and Physics, 18, 10557-
824 10574, 2018.
825 Yin, X., de Foy, B., Wu, K., Feng, C., Kang, S., and Zhang, Q.: Gaseous and particulate pollutants in
826 Lhasa, Tibet during 2013–2017: Spatial variability, temporal variations and implications,
827 Environmental Pollution, 253, 68-77, 2019.
828 Zhang, H., Fu, X., Lin, C., Wang, X., and Feng, X.: Observation and analysis of speciated atmospheric
829 mercury in Shangri-La, Tibetan Plateau, China, Atmos. Chem. Phys, 15, 653-665, 2015a.
830 Zhang, H., Fu, X., Lin, C.-J., Shang, L., Zhang, Y., Feng, X., and Lin, C.: Monsoon-facilitated

831 characteristics and transport of atmospheric mercury at a high-altitude background site in
832 southwestern China, Atmospheric Chemistry & Physics, 16, 2016.
833 Zhang, R., Wang, H., Qian, Y., Rasch, P. J., Easter, R. C., Ma, P.-L., Singh, B., Huang, J., and Fu, Q.:
834 Quantifying sources, transport, deposition, and radiative forcing of black carbon over the
835 Himalayas and Tibetan Plateau, Atmospheric Chemistry and Physics, 15, 6205-6223, 2015b.
836 Zhang, R., Wang, Y., He, Q., Chen, L., Zhang, Y., Qu, H., Smeltzer, C., Li, J., Alvarado, L., Vrekoussis,
837 M. J. A. C., and Physics: Enhanced trans-Himalaya pollution transport to the Tibetan Plateau by
838 cut-off low systems, 17, 2017.
839 Zhang, W., Tong, Y., Hu, D., Ou, L., and Wang, X.: Characterization of atmospheric mercury
840 concentrations along an urban–rural gradient using a newly developed passive sampler,
841 Atmospheric Environment, 47, 26-32, 10.1016/j.atmosenv.2011.11.046, 2012.
842 Zhou, H., Hopke, P. K., Zhou, C., and Holsen, T. M. J. S. o. t. T. E.: Ambient mercury source
843 identification at a New York State urban site: Rochester, NY, 650, 1327-1337, 2019.
844 Zhu, J., Xia, X., Che, H., Wang, J., Cong, Z., Zhao, T., Kang, S., Zhang, X., Yu, X., Zhang, Y. J. A. C.,
845 and Physics: Spatiotemporal variation of aerosol and potential long-range transport impact over
846 the Tibetan Plateau, China, 19, 14637-14656, 2019.
847